UC Davis
UC Davis Previously Published Works

Title

Multispectral analysis tools can increase utility of RGB color images in histology.

Permalink

Journal

ISSN

Authors

Fereidouni, Farzad
Griffin, Croix
Todd, Austin
et al.

Publication Date

DOI

Peer reviewed

Multispectral analysis tools can increase utility of RGB color images in histology

Farzad Fereidouni[1], **Croix Griffin**[2], **Austin Todd**[1], and **Richard Levenson**[1]

[1]Department of Pathology and Laboratory Medicine, University of California Davis, 4400 V Street, Sacramento, CA 95817, United States of America

[2]School of Veterinary Medicine, University of California Davis, 944 Garrod Drive, Davis, CA 95616, United States of America

Abstract

Multispectral imaging (MSI) is increasingly finding application in the study and characterization of biological specimens. However, the methods typically used come with challenges on both the acquisition and the analysis front. MSI can be slow and photon-inefficient, leading to long imaging times and possible phototoxicity and photobleaching. The resulting datasets can be large and complex, prompting the development of a number of mathematical approaches for segmentation and signal unmixing. We show that under certain circumstances, just three spectral channels provided by standard color cameras, coupled with multispectral analysis tools, including a more recent spectral phasor approach, can efficiently provide useful insights. These findings are supported with a mathematical model relating spectral bandwidth and spectral channel number to achievable spectral accuracy. The utility of 3-band RGB and MSI analysis tools are demonstrated on images acquired using brightfield and fluorescence techniques, as well as a novel microscopy approach employing UV-surface excitation. Supervised linear unmixing, automated non-negative matrix factorization and phasor analysis tools all provide useful results, with phasors generating particularly helpful spectral display plots for sample exploration.

Keywords

fluorescence; histopathology; phasor analysis; spectral imaging

1. Introduction

Multispectral imaging (MSI) initially became popular in the remote sensing community [1], and has in recent decades found multiple applications in biology and medicine, particularly when applied to microscopy. Benefits of MSI include enhanced detection of targets and improved signal-to-noise ratios because background (autofluorescent) signals can be spectrally unmixed from emissions arising from specific labels. MSI captures a spectrum of a signal at each pixel of an image and is applicable in transmission, reflectance and fluorescence modes. It is the higher-dimensional extension of familiar color (RGB) imaging,

levenson@ucdavis.edu.

which also captures spectral data (limited to three channels) at every pixel. For a recent review, see [2].

MSI is used to accomplish complex biomarker multiplexing in brightfield, and fluorescence images of tissue specimens [3, 4] as well as *in vivo* preclinical imaging [5]. It typically outperforms results obtainable using single band-pass filters, or simple color RGB sensors [2] viewed with simple tools. Autofluorescence, often viewed as an annoyance, can also be informative, as endogenous metabolites and macromolecules may generate useful signals in unstained specimens, both *in vivo* and *ex vivo* [6]. Clinically, dermatology is a field that has embraced MSI, along with other advanced optical techniques [7, 8]. Spectral imaging has also found application in intraoperative guidance for tissue viability (e.g. detecting oxygenation or perfusion) [9] or detection of biomarkers in surgical or endoscopic settings [10]. More general reviews of MSI and biomedical applications are available [11, 12]

The use of MSI comes with challenges. The instrumentation involved can be complex and expensive, and may employ tunable filters, or precisely controlled optical components such as those deployed in confocal microscopes [13]. MSI can also be inefficient in its use of light, requiring relatively longer exposure times than monochrome or simple color imaging methods. Such longer capture times reduce temporal resolution and may induce photobleaching or phototoxicity. Therefore, if it were possible to capture some of the discrimination power of MSI with more efficient capture methods, it could prove beneficial in terms of reduced complexity and increased speed [14, 15].

Managing and interpreting large multispectral data sets can also be difficult. Two basic tasks in working with such images include image classification of areas of interest, and signal unmixing, in which quantitative estimates of target abundances are arrived at. Classification relies on differences between spectra, and quantitation relies on mixing models which normally are assumed to be linear. (See the cited reviews for more complete discussion of spectral analysis tools.) Consequently, it is worth taking a look at what could be accomplished by combining easy-to-acquire 3-channel color images with analysis tools refined in the multispectral field.

Linear unmixing is one of the most widely utilized method, and can be used when the spectra of known species are available either from the dataset itself, via separate measurements, or obtained from the literature [16]. Relying on 'known' spectra can introduce errors into the analysis, as spectral properties can vary either due to environmental or other effects, or from variability introduced by the spectral measurement methods themselves. Analysis techniques based on prior knowledge will be less useful in cases in which characterization of accurate 'end-member' spectra may be imperfect. Numerous approaches have been developed to overcome this problem by applying constraints that allow for unmixing of the images with less *a priori* knowledge. Iterative minimum least-square (MLS) methods, non-negative matrix factorization (NMF) [17], or methods based on principal component analyses are approaches that analyze spectral data without reliance on previously characterized spectra [18].

A more recent development for exploring, as well as quantitatively analyzing, spectral data sets is a phasor-based approach. Phasors (a portmanteau of phase vector) found original application in the analysis of electrical circuits, telecommunications and other situations [19]. More recently, the technique was applied to biomedical imaging, initially in the analysis of fluorescence lifetime imaging microscopy [20, 21]. Extension of this method from the time to the spectral domain was subsequently demonstrated [22–24]. Advantages of the phasor approach include its ability to provide an easy-to-interpret graphical representation for visualization of the data in a 2D (or higher dimension if necessary) space. This happens as each spectrum is converted into a vector and shown as a single point on the resulting plot (figure 1). The superposition of spectra on a pixel level follows the vectorial summation rule of individual vectors on the phasor plot, providing a straightforward tool for both segmentation and unmixing of individual components. Phasors have been used in biomedical applications to distinguish different components in human skin *in vivo* [8], identifying specific RNA subspecies in live cells [23] and segmentation of cell compartments using Raman spectra [25], to name a few. This method is applicable when using as few as three spectral channels [22].

Comparison of MSI and RGB imaging for evaluation of HER2 status on breast cancer cells has been reported previously [26]. Here, we first provide a brief introduction to phasor analysis, illustrate its application to an information-rich remote sensing dataset, and show that reduction from >400 bands down to three bands preserves most of useful spectral features. We then model the accuracy of spectral imaging devices with different number of spectral bands in a wide-field imaging configuration. Finally, we examine use-cases of more relevance to microscopy: brightfield multiplexed imaging, a fluorescence image of mouse small intestine, and finally, an example of a new microscopy method employing short-wavelength UV surface excitation. These examples are analyzed using the three different multispectral tools previously mentioned (MLS, NMF and phasors), and illustrate that considerable utility can be achieved from RGB images alone.

2.   Materials and methods

2.1.   Phasor analysis

Phasor analysis was performed using an ImageJ plugin developed by the first author, freely available at the website www.Spechron.com and fully described elsewhere [22]. In this method, the sine and cosine transformation of spectra are plotted on a two-dimensional scatter plot with the cosine transform on the horizontal axis and the sine transformation on the vertical axis. The spectrum peak position is encoded as points projected onto the unit circle, and bandwidth determines the radial distance from the center. Phasor plots of complex image data can be displayed using a density-mapped color look-up-table, as shown in figure 2. Phasor-based unmixing was compared with other established techniques for multispectral image analysis, including NMF and Nuance™ spectral image analysis software (PerkinElmer, Waltham, MA) which is based on MLS.

2.2. Theoretical error analysis

Simulations were performed with Mathcad (PTC, Needham, MA 02494, USA). A Fisher information matrix [27] was used to analytically calculate the variance in measuring spectral width. Analysis was restricted to the most widely used MSI configuration in which spectral bands are acquired in a consecutive format either using tunable filters or bandpass filter wheels [28], while discarding light emitted in out-of-band wavelengths. Such techniques can be faster and optically simpler than point-scanning methods. Spectral bandwidths of the captured spectra and number and width of the instrument bandpass filters were then systematically varied and effects on accuracy of estimation of spectra determined. Assuming a Gaussian spectrum with spectral width σ, recorded with a system with k spectral channels and a total spectral detection range L, the collected photons per each spectral channel N_i are calculated by:

$$N_i = N_0 \int_{i\frac{L}{k}}^{(i+1)\frac{L}{k}} e^{-\frac{(l-L/2)^2}{2\sigma^2}} \qquad (1)$$

$$= \sqrt{2\pi}\sigma \frac{\mathrm{erf}\left(\frac{\sqrt{2}L}{4k\sigma}(k-2i+2)\right) - \mathrm{erf}\left(\frac{\sqrt{2}L}{4k\sigma}(k-2i)\right)}{2}.$$

i is the index for the spectral channel and N_0 is the number of photons arriving at the filter element. The total number of photons arriving at the sensor is calculated as above by replacing the integration limit from 0 to L. The probability of detecting photon P_i at each spectral channel is calculated by dividing the N_i over the total number of photons:

$$p_i = N_0 \frac{\mathrm{erf}\left(\frac{\sqrt{2}L}{4k\sigma}(k-2i+2)\right) - \mathrm{erf}\left(\frac{\sqrt{2}L}{4k\sigma}(k-2i)\right)}{2\mathrm{erf}\left(\frac{\sqrt{2}L}{4\sigma}\right)}. \qquad (2)$$

The calculation above assumes that the counts at all spectral channels are recorded simultaneously. However, in systems in which the spectrum is recorded in sequential mode, the exposure time of each channel is scaled inversely with k. In order to have a fair comparison between the systems with different number of spectral channels, all acquisitions should be accomplished within the same total exposure time. Thus, equation (2) needs to be corrected as follows:

$$p_i = \frac{N_0}{k} \frac{\mathrm{erf}\left(\frac{\sqrt{2}L}{4k\sigma}(k-2i+2)\right) - \mathrm{erf}\left(\frac{\sqrt{2}L}{4k\sigma}(k-2i)\right)}{2\mathrm{erf}\left(\frac{\sqrt{2}L}{4\sigma}\right)}. \qquad (3)$$

Note that this parameter does not take into account the detector efficiency at different spectral channels and assumes that the sensitivity is equal over the whole spectral range.

The variance of estimate of spectral width is calculated by [27]:

$$\mathrm{var}(\sigma) = \frac{1}{N_0}\left(\sum_i \frac{1}{p_i}\frac{\mathrm{d}p_i^2}{\mathrm{d}\sigma}\right)^{-1}. \quad (4)$$

In order to investigate the sensitivity of the system and to compare different settings, a figure of merit F [29] was calculated. F does not depend on the number of detected photons and its magnitude is always larger than 1. Moreover, lower values of F correspond to higher sensitivities for spectral width measurements. F is defined as:

$$F = \frac{\Delta\sigma}{\sigma}\frac{\Delta N_0}{N_0}. \quad (5)$$

It is assumed that the $\Delta\sigma/\sigma$ and $\Delta N_0/N_0$ are governed by Poisson statistics. Therefore, we can rewrite F as:

$$F = \frac{\sqrt{\mathrm{var}(\sigma)}}{\sigma}\sqrt{N_0}. \quad (6)$$

Note that N_0 is not the number of photons actually collected at the sensor, which may be a much smaller number. The required number of photons for a desired error is calculated as follows:

$$N_0 = \frac{F^2}{(\text{desired error})^2}. \quad (7)$$

2.3. Microscopy approach employing UV-surface excitation (MUSE) and sample imaging

The description for the optical setup (MUSE) can be found elsewhere [30, 31]. Briefly, the setup comprises a custom-built wide-field microscope with a relatively deep UV (280 nm) excitation source that illuminates a stained sample in free-space oblique mode, avoiding the need for UV-transmissive optics. A 10× (NA 0.45) objective (Nikon, Japan) is employed for imaging. The images were recorded with a 9-MP scientific-grade color camera (Ximea, MD091CU-S5, Germany).

2.4. Histology examples

Brightfield: A conventionally processed human lymph node containing small metastatic cancer deposits was stained with an antibody targeted to AE1/AE3 cytokeratin, visualized with Fast Red chromogen, and CD3 cells were visualized with an anti-CD3 antibody and

DAB. Nuclei were counter stained with hematoxylin. The color image was obtained using a Nuance multispectral camera, and the resulting dataset was converted to an RGB image using a CIE-based color mapping.

Fluorescence: A mouse small intestine cryosection showing Paneth and goblet cells labeled with Alexa Fluor® 594 wheat germ agglutinin, and the microvillar brush border and smooth muscle layers labeled with Alexa Fluor® 488 phalloidin. Nuclei were labeled with DAPI. The specimen was excited with a 350/50 excitation filter coupled with a long-pass dichroic and 510 nm long-pass emission filter. A multispectral camera (Nuance, CRI) was used to collect the data and an RGB color image was synthesized using a typical RGB bandpass matrix.

MUSE thick-tissue microscopy: A specimen was obtained from the dermal component of a Patnaik grade III, Kiupel high-grade canine cutaneous mast cell tumor which had been stored in 10% buffered formalin for approximately six months. The tumor had been removed from a 6-year-old Great Dane and proved to be a poorly demarcated, infiltrative, moderately cellular mass comprised of small clusters and individual mast cells infiltrating the mid and deep dermis and panniculus. The tissue slice was faced by hand using a scalpel and stained with 0.04% aqueous berberine (berberine hemisulfate salt $> = 95\%$, Sigma-Aldrich) titrated to pH 3.0 with citric acid for 5 min with occasional manual agitation. The sample was then rinsed in distilled water at 24 °C and pH 6.80 for 5 min and then directly placed onto a UV-transparent stage on the MUSE system and imaged. A section of the same tumor was processed for regular histology and stained with toluidine blue to highlight the mast cells.

3. Results

3.1. Phasor plots at different spectral resolutions

Figure 1(A) shows the effect on phasor point location position for Gaussian spectra of varying their peak position from the first spectral channel to the last spectral channel and for different spectral band widths. Figure 1(B) demonstrates the spectral mixing concept on a phasor plot. Three pure spectra shown in red, green and blue in phasor space. The phasor transforms of all possible superposition of these spectra fall inside the triangle whose vertices are the phasor points of the pure spectra. As an example, the phasor vector from an equal contribution from all three pure spectra falls exactly in the middle of the triangle. Unmixing can be performed by measuring the area formed by the total phasor vector made by the other vertex as shown in the figure 1(B). Figures 1(C) and (D) show the same spectral modifications as in 1(A), but with the number of spectral channels binned to eight and three channels respectively. No significance change is observed when binning to eight channels but the phasor plot for a 3-spectral-channel system shows overlap between the sharp spectra measured close to the edge of spectral detection window. For many biological applications, this is of less importance, as most of the spectra shows large band widths and their phasors fall in the middle of the plot and thus are more easily distinguishable. Additional harmonics can be used to increase the spectral fidelity of the phasor transform, but in the present case, only the first harmonic is used [32].

3.2.   Spectral phasor analysis of remote sensing data

As an example of application of spectral phasor method for analysis of spectral data, we used a spectrally and spatially complex aerial scan of landscape located near San Joaquin, CA, downloaded from http://neondataskills.org/ [33]. The image was acquired using 426 wavelength bands from 380 to 2510 nm.

The RGB reconstruction of the image was performed using data from visible wavelengths; roads, various forms of vegetation and soil are evident (figure 2(A)). The complex spectra reflected by different features are shown in figure 2(B) with the result of the phasor transformation of the entire spectral image demonstrated in figure 2(C). Pixels with similar spectral properties are collected in a same region on the phasor plot and forms clusters, with color stemming from a look-up table for pixel abundance across the phasor plot. Image segmentation can be accomplished by selecting phasor clusters—which then map back to the original image. Different features are clearly highlighted, as indicated. The reciprocal property of the phasor plot allows for straightforward segmentation without any *a priori* knowledge. By exploring additional clusters on the phasor plot it is possible to extract other features as well, such as the soil, specific types of vegetation, and walking paths (figures 2(D)–(H)). Figure 2(I) shows a phasor plot in which the spectral data had been binned from >400 down to only three channels. Separations of clusters in 2(I) versus (C) show slight degradation (compare regions D and G, or F), but the 3-channel version preserves most of the discrimination power. This suggests that 3-channel imaging and unmixing may be useful in a variety of settings. In addition to segmentation, phasor clusters or scatter-plot vertices can also serve as inputs for spectral unmixing, as shown in [22].

3.3.   Interrelationship of image content and spectral resolution with noise

Spectra of many fluorescent emitters in biological specimens are typically broad, with full-width at half maximum (FWHM) in the range of 40 nm [34]. Consequently, it may be possible to collect spectral information using broader band passes are often used. Not infrequently, for example, users of tunable-filter-equipped systems collect wide-spectral range data sets with images stepped every 10 nm, simply because that is the default setting in systems such as the Nuance MSI system (*PerkinElmer*) (RL, personal observation). As shown below, such strategies greatly increase the number of photons required for low-noise unmixing. It is possible that simple 3-channel, broad-bandwidth detectors, such as simple color cameras, can be suitable in the limiting case where there are only three targets of interest.

Using the model described here, we sought the figure of merit for estimation of spectral width of spectra recorded in sequential mode for a total spectral acquisition window of 250 nm. This is an important metric because correct estimates of end-member spectra are required for accurate unmixing. The number of spectral channels and the width of simple Gaussian spectra were varied and figure-of-merit curves were generated (figure 3). As can be seen, using larger numbers of spectral collection channels allows for accurate width estimation for narrow (<20 nm) spectra; however the figure of merit for detection of such a narrow spectrum worsens when using fewer detection channels, reflecting a need to collect more photons, and thus a requirement for longer acquisition times. On the other hand, when

the spectral band width of the signals is large (>40 nm) as is the case for many fluorescent dyes used in biological imaging, fewer channels and thus fewer photons are needed. This can be inferred from the lower figure of merit for spectral band widths larger than 40 nm. As can be seen, good accuracy can in fact be achieved with as few as three channels (for example, R, G, and B). Using equation (7) we estimate that this requires approximately 7× fewer photons than a system using 32 channels for correctly estimating a spectrum with FWHM of 60 nm. This large difference can be explained by the operation of two loss mechanisms: first, having more spectral channels means that narrower bandpass filters are deployed, thus discarding a greater percentage of total photons with each capture; second, increasing the number of recorded channels captured within a given exposure time necessarily reduces individual exposure times for each channel. While this analysis addresses sequential image capture mode, a Bayer-pattern-color sensor provides essentially the same photon economy and can be simpler, smaller and less expensive than alternative sensors. It should be noted that the case of Bayer (or other spatially interpolated spectral sensors), there is a trade-off between spectral and spatial resolution. As long as the pixels are pitched to capture the scene at better than Nyquist sampling rate, the impact on resolution and unmixing should be negligible, except perhaps in the case of sharp edges [35].

3.4. Imaging lymph node with metastatic cancer in brightfield mode

An RGB image of a lymph node with metastatic cancer deposits is shown in figure 4(A). Figure 4(B) shows the same image converted to absorbance (optical density) rather than transmittance, a data transformation required for effective spectral unmixing [36]. A phasor plot of the image (figure 4(C)) was generated using an ImageJ-based phasor plugin; its triangular shape indicates the presence of three major spectral components. By manually selecting the vertices on this plot for unmixing, three components with minimum overlap could be unmixed, as shown in figures 5(G)–(I). The image was also analyzed using two other approaches for unmixing: NMF [13] and supervised MLS using a 'compute-pure-spectra' function available in Nuance software and originally described by Levenson and Mansfield [3]. In fact, all three of these methods are seeking the best estimates of end-member spectra. The actual unmixing step for all of them uses a linear model after definition of appropriate end-member spectra. Unmixing results are largely similar for this relatively simple 3-color image.

3.5. Mouse intestine cryosection imaged with a fluorescence microscope

The color image resulting from an RGB distillation of an original spectral data set was analyzed using the three spectral tools employed in the previous example. The three unmixed images consist of the villus border (figure 5, left column), combination of nuclei (too small at this magnification to individually resolve) and autofluorescence (figure 5, center column), and Paneth and goblet cell mucins (figure 5, right column). The three RGB unmixing approaches yield generally similar results, with MLS apportioning more of the signal to the nuclei + AF central channel, NMF distributing more of the central channel signal to the other channels, and the phasor method appearing to split the difference. Spectral unmixing of the original multispectral data (not shown) provided results most similar to MLS, which is not surprising since the same software and compute-pure-spectrum methodology was used in both cases.

3.6. Mast cell tumor imaged via MUSE

Finally, we applied the three different spectral analysis tools to an RGB-color image of a surgical resection specimen from a canine mast cell tumor stained with a single fluorescent dye, and subjectively compared the quality of the unmixing results. Unmixing fidelity is important, since both quantification of heparin content and assessment of nuclear size and shape are part of tumor grading. The standard stain for mast cell tumors after conventional histology processing is toluidine blue; this relies on the metachromasia of the dye [37] as heparin granules stain violet in contrast to the blue nuclei.

An image of a canine cutaneous mast cell tumor stained with berberine was captured using UV surface excitation microscopy (MUSE). Figure 6 indicates the resulting RGB image, 3-band 'spectra' from three different regions of interest, and the phasor scatter plot. Berberine causes most of the specimen to fluoresce in green while the stained mast cell granules emit a yellow signal. The green-staining region, however, comprises two major components: nuclei and stroma that are difficult to resolve by eye. Figure 4(B) shows 3-channel spectra from manually selected stroma, nuclei and mast-cell cytoplasm regions and the phasor plot from the entire image is shown in figure 4(C).

As can be seen in figure 7, similar unmixing results were obtained with all three tools, but some significant differences can be discerned. The first row ((A)–(C)) shows the results of unmixing using supervised, manually computed pure spectra with Nuance spectral analysis software (MLS). Three components are separated but the signal from collagen and other stromal components in figure 7(A) includes substantial crosstalk contribution from nuclear components (see unmixed into (B)). This reflects imperfect estimation of spectral end-members for the unmixing, which may be due to extensive spatial overlap of nuclei and stroma. Figure 7(C) shows stained mast cell granules, exhibiting minimal crosstalk from other channels.

The results from NMF are shown in figures 7(D)–5(F). While the stromal signals in figure 7(D) do not show as much contamination with nuclear components as seen in figure 7(A), mast cell granule unmixing results in holes (highlighted by arrows) corresponding to regions of relatively intense mast-cell granule staining signals. Note the textured patterns in figures 7(D) and (G) that reveal the presence of swirling collagen fibers not visible in the unmixed figure 7(A).

Finally, phasor analysis resulted in unmixing of components with minimum cross-talk. The stromal image contains little or no contamination from nuclear components. We still do see some contamination of the regions with high mast-cell granule signals, but less than seen with NMF. However, some stromal signals do appear in the nuclear channel in figure 5(H). Figure 5(I) demonstrates good delineation of the mast cell-granule signals. The lowest row in figure 5 shows details indicating that berberine metachromasia reflects binding to heparin and is generally seen to surround the nuclei, its expected location, mimicking the results seen with toluidine stain (figure 7(M)), shown in the brightfield mode.

4. Conclusion

High-resolution spectral imaging techniques can be appropriate for addressing signal detection in multiplexed, fluorescently labeled specimens. This is currently of great interest for characterizing immune-oncology-relevant phenotypes [38], as well as other situations in which fewer signals of interest may be present. We present evidence that much can be accomplished using simple RGB color sensors, accompanied by straightforward segmentation and/or unmixing methods. The ability to collect the image quickly, as compared to multiple band-sequential acquisitions, can reduce the possibility of phototoxicity and photobleaching, and shorten overall imaging times.

In biological unmixing situations, general tissue stains that bind across a whole specimen generate signals that may be mixed with widely present autofluorescence. It can be challenging to determine the accurate spectral end-members required for low-error unmixing into individual components and to separate useful signal from noise. In other words, reference spectra and unwanted noise may not be spectrally independent or known. The challenge is to extract these signals from the image itself.

A number of manual (supervised), semi-automated, and automated tools have been developed for such a task. We compared phasors to two commonly used methods. NMF, widely used in chemometrics, is an automated tool that automatically seeks end-members based in part on non-negativity constraints, reflecting the notion that mixture constituents cannot be present at concentrations lower than zero. Supervised spectral unmixing using the 'compute-pure spectra' approach can generate end-member spectra in which spectra that are composed of more than one end-member are decomposed into pure estimates prior to unmixing. The phasor approach helps visualize the presence of different spectral components, and in favorable situations, the vertices generate end-member estimates that support accurate unmixing—up to three components from an RGB image. Compared to statistically-based tools such as principal component analysis, phasor plot shapes do not depend on spectral species abundance, only on actual spectral content, meaning that phasor-determined clusters or end-members will be applicable to any image acquired under similar conditions, regardless of species abundance.

The mast cell tumor presented here stained with berberine and imaged using MUSE posed a challenging unmixing problem, as fluorescent signals were not spectrally distinct. The staining method is based on the use of berberine on standard histology sections combined with traditional fluorescence microscopy for the staining and quantification of heparin in mast cell granules [39, 40]. Berberine has four absorption peaks between 200 and 450 nm and one emission peak at 565 nm. This allowed the brilliant yellow–green cytoplasm and green nuclei of mast cells (and green nuclei of other cell types) that Enerback described on traditional fluorescence microscopy to be visible on thick tissue sections using MUSE-based UV-excitation at around 280 nm. Differential staining and phasor unmixing was able to demonstrate the shape and size of the mast cells and their nuclei, and could indicate tumor grade, an important feature that determines appropriate surgical management [37, 41].

This report demonstrates that a strategy based on full color brightfield and fluorescence imaging, including MUSE, coupled with appropriate analysis and unmixing tools can provide a surprisingly simple and robust alternative to more complex multispectral approaches for rapid imaging and potentially intraoperative assessment. In the future, this general approach can be studied for suitability in a wide variety of clinical and research tissue imaging tasks.

Acknowledgments

References

[1]. Solomon J and Rock B 1985 Imaging spectrometry for earth remote sensing Science 228 1147–52 [PubMed: 17735325]

[2]. Bearman G and Levenson R 2003 Biological imaging spectroscopy Biomedical Photonics Handbook ed Vo-Dinh T (Boca Raton, FL: CRC Press) pp 8_1–26

[3]. Levenson RM and Mansfield JR 2006 Multispectral imaging in biology and medicine: slices of life Cytometry A 69 748–58 [PubMed: 16969820]

[4]. Taylor CR and Levenson RM 2006 Quantification of immunohistochemistry—issues concerning methods, utility and semiquantitative assessment II Histopathol 49 411–24

[5]. Gao X et al. 2004 In vivo cancer targeting and imaging with semiconductor quantum dots Nat. Biotechnol 22 969–76

[6]. Palero JA et al. 2011 In vivo monitoring of protein-bound and free NADH during ischemia by nonlinear spectral imaging microscopy Biomed. Opt. Express 2 1030–9 [PubMed: 21559117]

[7]. Derek H,EK and Jagdeo J 2016 Richard Levenson Spectral Imaging in Dermatology in Imaging in Dermatology ed Gupta MHPAG (New York: Academic) pp 217–39

[8]. Fereidouni F et al. 2014 Phasor analysis of multiphoton spectral images distinguishes autofluorescence components of in vivo human skin J. Biophotonics 7 589–96 [PubMed: 23576407]

[9]. Basiri A et al. 2010 Use of a multi-spectral camera in the characterization of skin wounds Opt. Express 18 3244–57

[10]. Yang VX et al. 2003 A multispectral fluorescence imaging system: design and initial clinical tests in intra-operative photofrin-photodynamic therapy of brain tumors Lasers Surg. Med 32 224–32 [PubMed: 12605430]

[11]. Lu G and Fei B 2014 Medical hyperspectral imaging: a review J. Biomed. Opt 19 010901

[12]. Gao L and Smith RT 2015 Optical hyperspectral imaging in microscopy and spectroscopy—a review of data acquisition J. Biophotonics 8 441–56 [PubMed: 25186815]

[13]. Sinclair MB et al. 2006 Hyperspectral confocal microscope Appl. Opt 45 6283–91 [PubMed: 16892134]

[14]. Neher R and Neher E 2004 Optimizing imaging parameters for the separation of multiple labels in a fluorescence image J. Microsc 213 46–62 [PubMed: 14678512]

[15]. Esposito A, Popleteeva M and Venkitaraman AR 2013 Maximizing the biochemical resolving power of fluorescence microscopy PLoS One 8 e77392 [PubMed: 24204821]

[16]. Dickinson ME. et al. 2001; Multi-spectral imaging and linear unmixing add a whole new dimension to laser scanning fluorescence microscopy. BioTechniques. 31:1272. [PubMed: 11768655]

[17]. Neher RA et al. 2009 Blind source separation techniques for the decomposition of multiply labeled fluorescence images Biophys. J 96 3791–800 [PubMed: 19413985]

[18]. Ropodi AI, Panagou EZ and Nychas G-JE 2017 Multispectral imaging (MSI): a promising method for the detection of minced beef adulteration with horsemeat Food Control 73 57–63

[19]. Fox H and Bolton W 2002 Mathematics for Engineers and Technologists (Woburn, MA: Butterworth-Heinemann)

[20]. Digman MA et al. 2008 The phasor approach to fluorescence lifetime imaging analysis Biophys. J 94 L14–6 [PubMed: 17981902]

[21]. Fereidouni F et al. 2011 A modified phasor approach for analyzing time-gated fluorescence lifetime images J. Microsc 244 248–58 [PubMed: 21933184]

[22]. Fereidouni F, Bader AN and Gerritsen HC 2012 Spectral phasor analysis allows rapid and reliable unmixing of fluorescence microscopy spectral images Opt. Express 20 12729–41 [PubMed: 22714302]

[23]. Andrews LM et al. 2013 Spectral phasor analysis of Pyronin Y labeled RNA microenvironments in living cells Biomed. Opt. Express 4 171–7 [PubMed: 23304656]

[24]. Cutrale F et al. 2017 Hyperspectral phasor analysis enables multiplexed 5D in vivo imaging Nat. Methods 14 149–52 [PubMed: 28068315]

[25]. Fu D and Xie XS 2014 Reliable cell segmentation based on spectral phasor analysis of hyperspectral stimulated Raman scattering imaging data Anal. Chem 86 4115–9 [PubMed: 24684208]

[26]. Liu W et al. 2016 A Comparative performance analysis of multispectral and RGB imaging on HER2 status evaluation for the prediction of breast cancer prognosis Trans. Oncol 9 521–30

[27]. Köllner M and Wolfrum J 1992 How many photons are necessary for fluorescence-lifetime measurements? Chem. Phys. Lett 200 199–204

[28]. Levenson RM 2006 Spectral imaging perspective on cytomics Cytometry A 69 592–600 [PubMed: 16680703]

[29]. Gerritsen H et al. 2002 Fluorescence lifetime imaging in scanning microscopes: acquisition speed, photon economy and lifetime resolution J. Microsc 206 218–24 [PubMed: 12067366]

[30]. Fereidouni F. et al. 2015; Microscopy with UV surface excitation (MUSE) for slide-free histology and pathology imaging. SPIE BiOS (International Society for Optics and Photonics). doi: 10.1117/12.2080408)

[31]. Fereidouni F et al. 2017 Microscopy with ultraviolet surface excitation for rapid slide-free histology Nat. Biomed. Eng 1 957–66 [PubMed: 30416866]

[32]. Cutrale F, Salih A and Gratton E 2013 Spectral Phasor approach for fingerprinting of photo-activatable fluorescent proteins Dronpa, Kaede and KikGR Methods Appl. Fluorescence 1 035001

[33]. Network NEO 2017 Data Products: [D17]. Provisional data on 2017: Battelle, Boulder, CO

[34]. Lakowicz J R 2013 Principles of Fluorescence Spectroscopy (New York: Springer)

[35]. Farsiu S, Elad M and Milanfar P 2006 Multiframe demosaicing and super-resolution of color images IEEE Trans. Image Process 15 141–59

[36]. Ruifrok AC and Johnston DA 2001 Quantification of histochemical staining by color deconvolution Anal. Quant. Cytol. Histol 23 291–9 [PubMed: 11531144]

[37]. Patnaik A, Ehler W and MacEwen E 1984 Canine cutaneous mast cell tumor: morphologic grading and survival time in 83 dogs Veterinary Pathol 21 469–74

[38]. Carstens JL. et al. 2017; Spatial computation of intratumoral T cells correlates with survival of patients with pancreatic. cancer Nat. Commun. 8:15095. [PubMed: 28447602]

[39]. Enerbäck L 1974 Berberine sulphate binding to mast cell polyanions: a cytofluorometric method for the quantitation of heparin Histochem. Cell Biol 42 301–13

[40]. Dimlich RV et al. 1980 The fluorescent staining of heparin in mast cells using berberine sulfate: compatibility with paraformaldehyde or o-phthalaldehyde induced fluorescence and metachromasia Stain Technol 55 217–23 [PubMed: 6160648]

[41]. Welle MM et al. 2008 Canine mast cell tumours: a review of the pathogenesis, clinical features, pathology and treatment Veterinary Dermatol 19 321–39
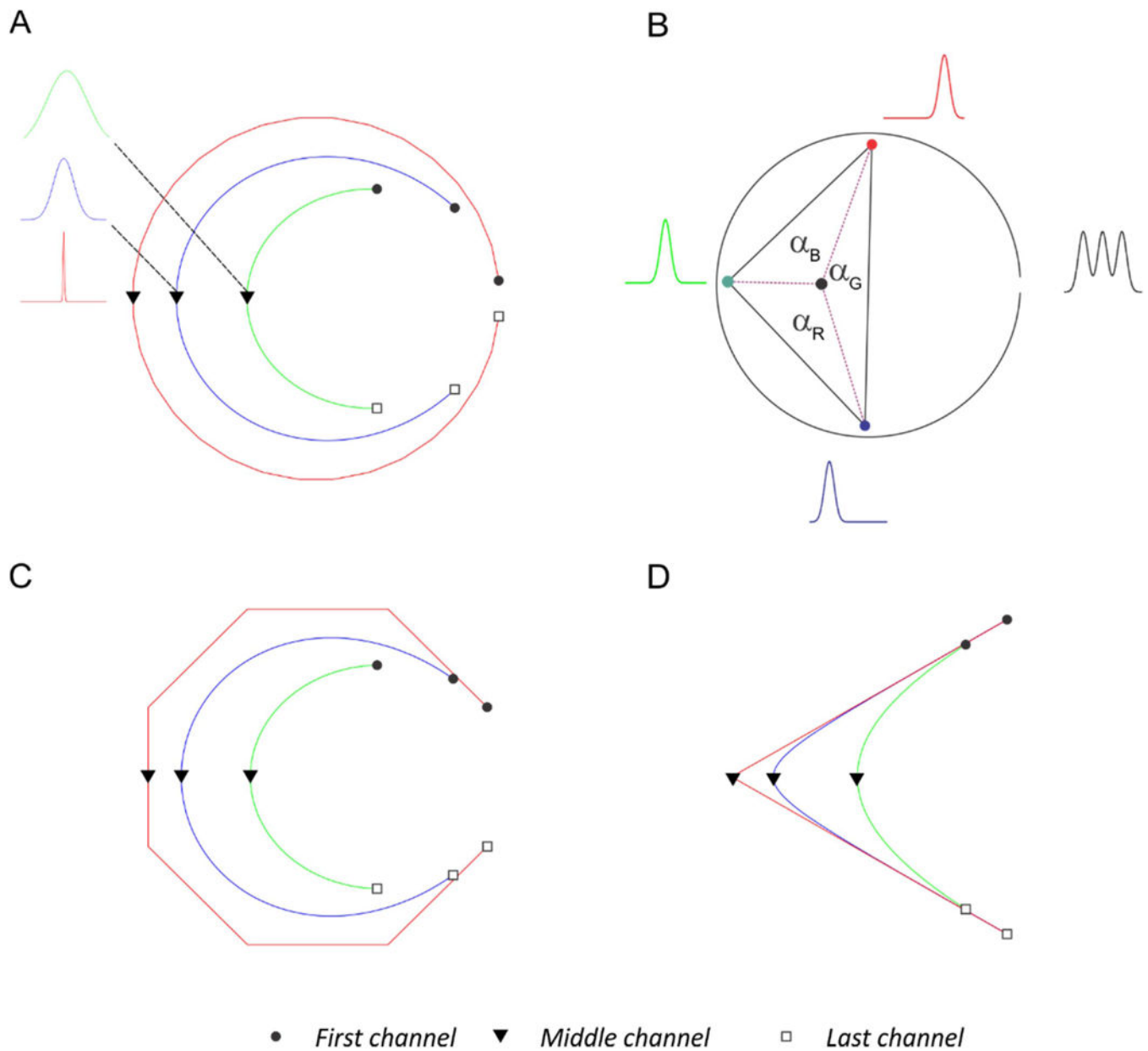
Figure 1.
Phasor encoding of multiple Gaussian spectra with different peak positions and band widths. Each spectrum is converted into a point on a phasor plot. Changing the peak position moves the phasor position around a circle and changing the bandwidth moves the point radially. (B) Visualization of spectral mixing on a phasor plot. The black spectrum is the superposition of the red, green and blue spectra. Note that the its phasor position falls in the middle of the triangle formed by the phasor positions of the three pure spectra. The fractional intensities from these spectra a_B, a_G and a_R are calculated by finding the area shown. (C), (D) The same spectral modifications as in (A), but with the number of spectral channels binned to eight and three channels, respectively.
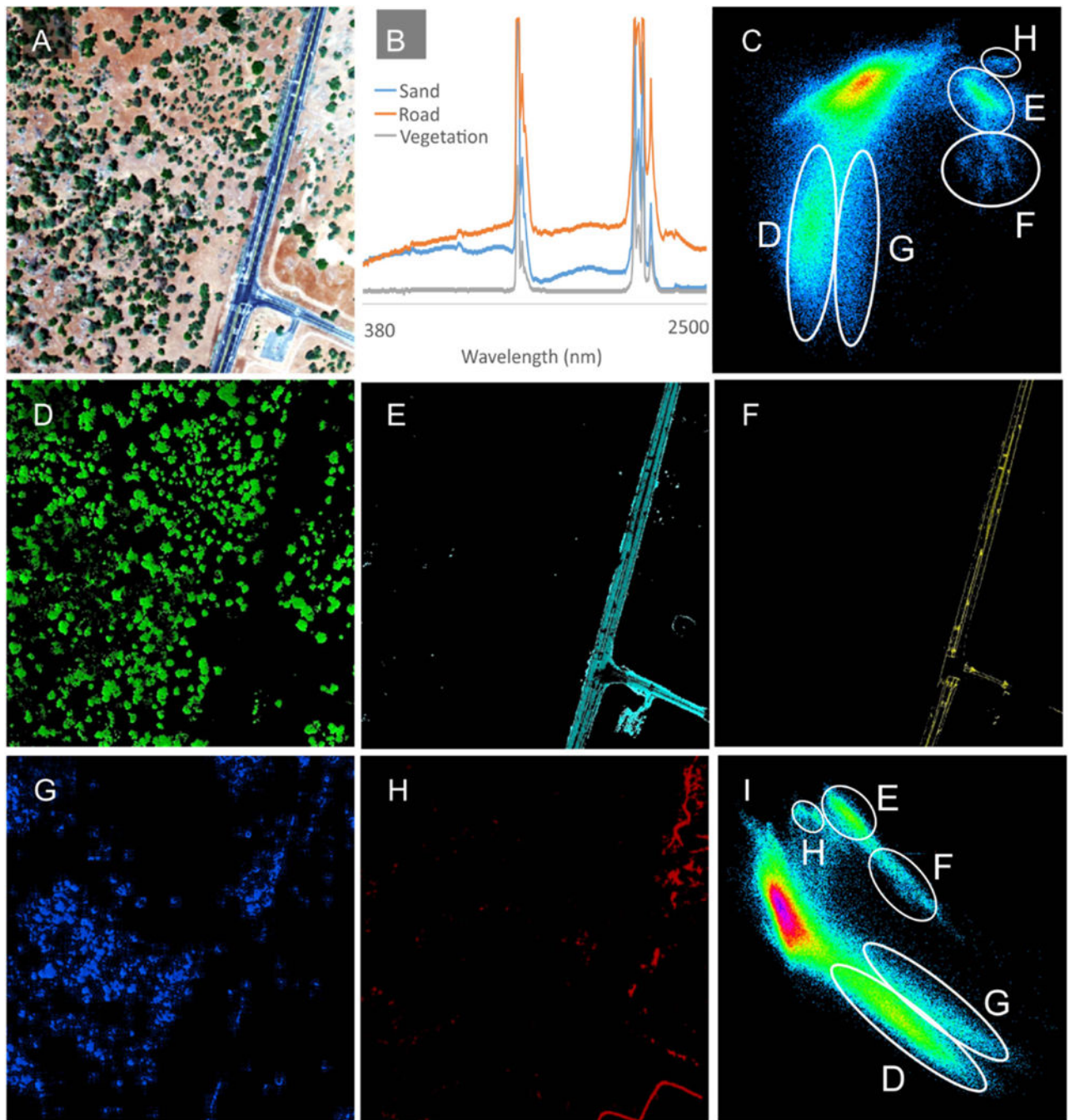
Figure 2.
(A) The RGB conversion from the visible bands. (B) Spectra of sand, road and vegetation
(C) the phasor plot of the image and segmented areas (D) vegetation, (E) roads, (F) lanes,
(G) vegetation and (H) walking paths. (I) The phasor plot of the image binned to three
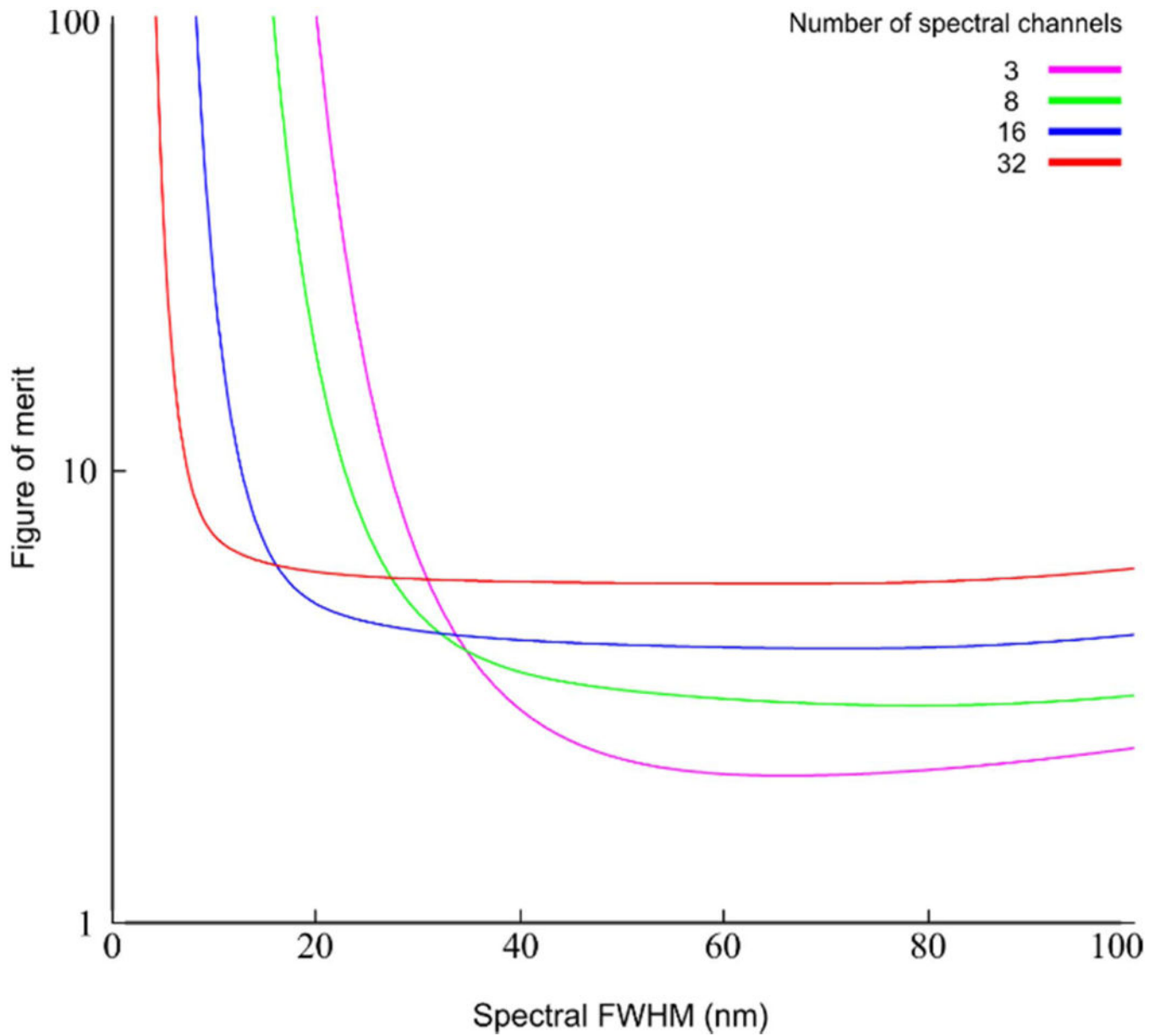channels.

Figure 3.
Figure of merit for estimation of spectral width with spectrographs with 3, 8, 16 and 32 channels acquired in widefield scheme.
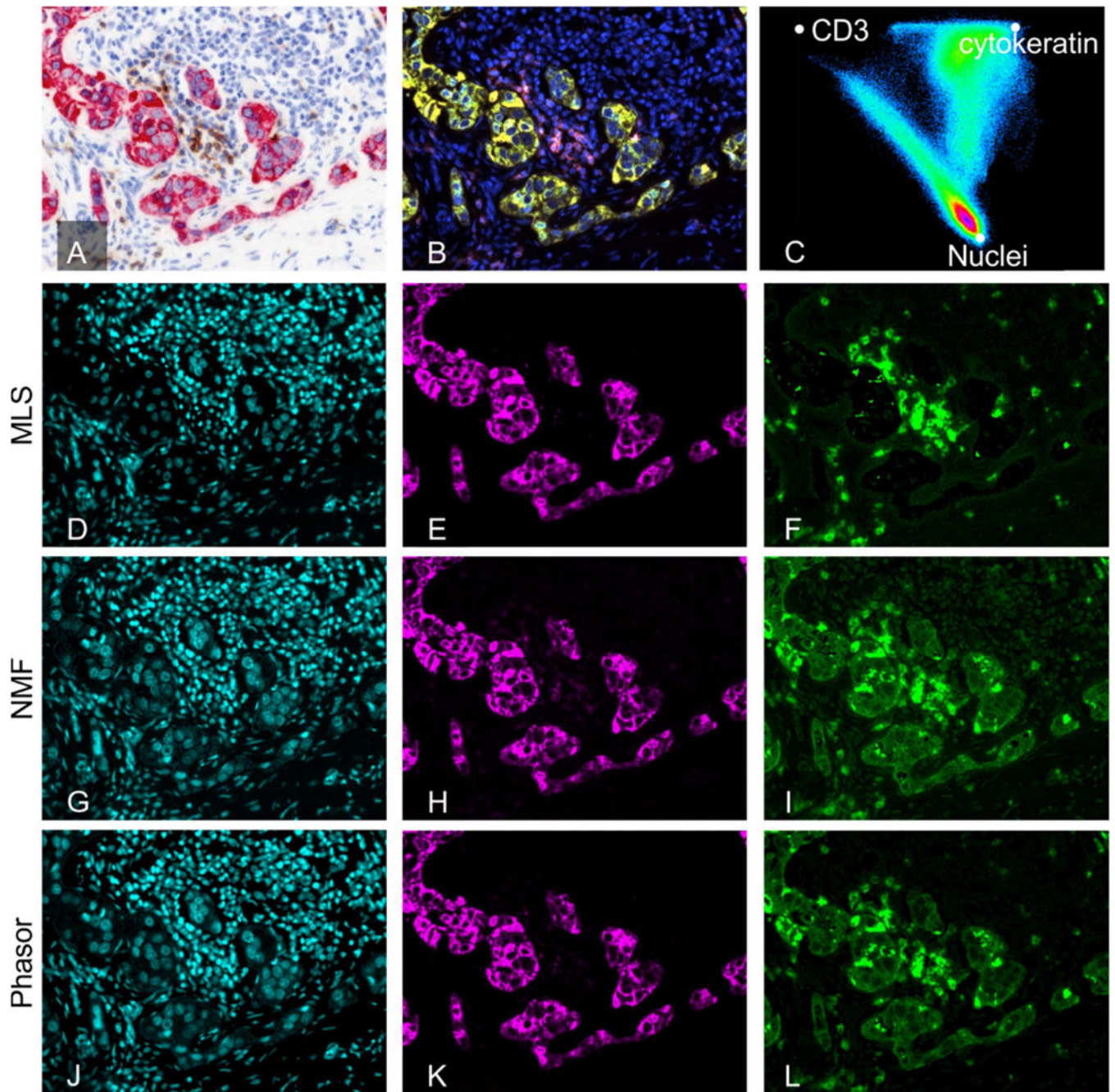
Figure 4.
(A) Bright field image of Lymph node with metastatic cancer. (B) Converted optical density image. (C) Phasor plot of the image indicating presence of three components. Unmixing result for nuclei (D), (G), (J) cytokeratin (E), (H), (K) and CD3 (F), (I), (L) from MLS, NMF and phasor approach, respectively.
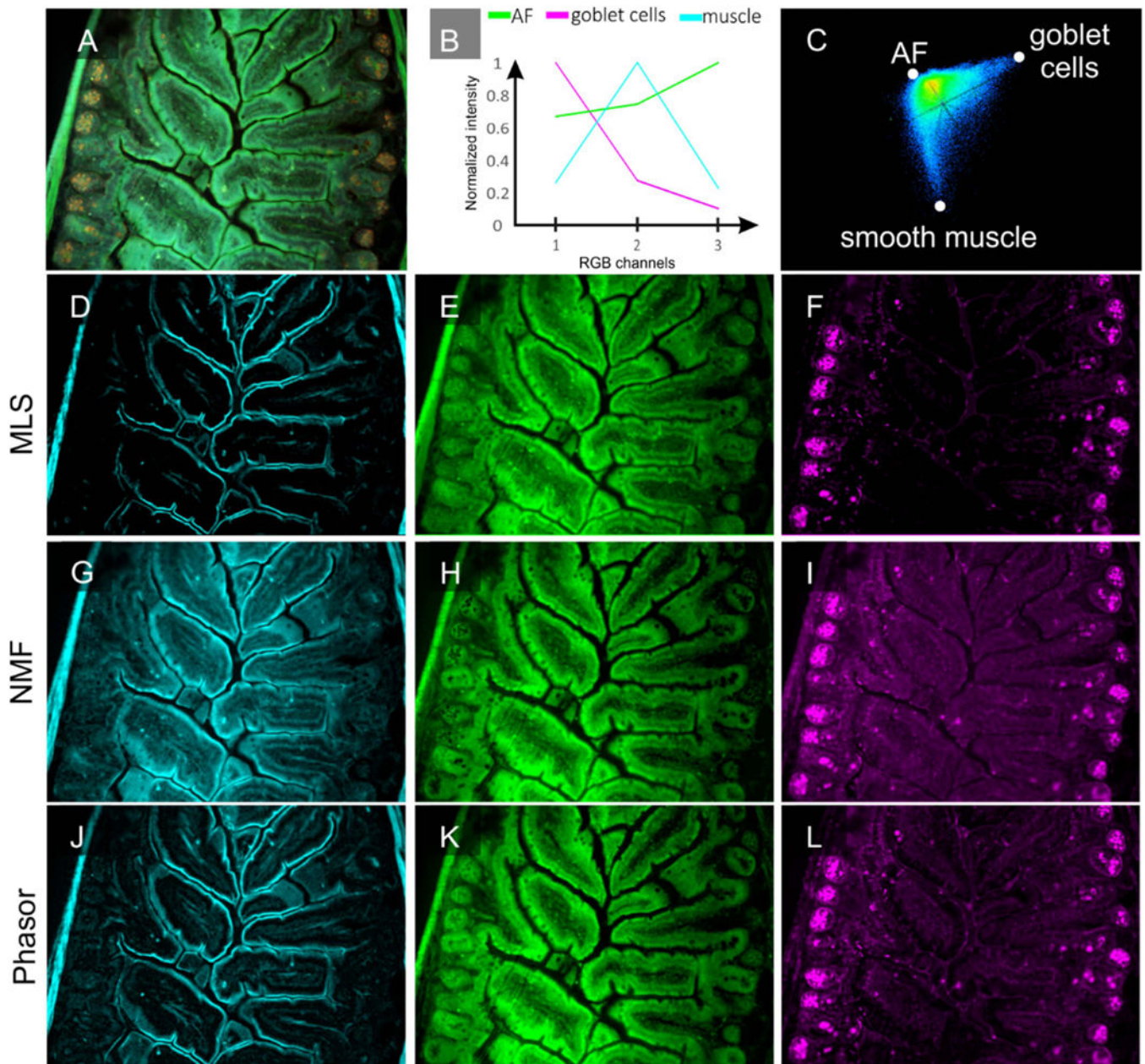
Figure 5.

(A) Fluorescence image of cryosectioned mouse small intestine. (B) Computed spectra after compute-pure-spectrum steps to estimate pure spectral components. (C) Phasor plot, indicating vertices reflecting spectral signatures of autofluorescenc, goblet cells and smooth muscle, villus border.
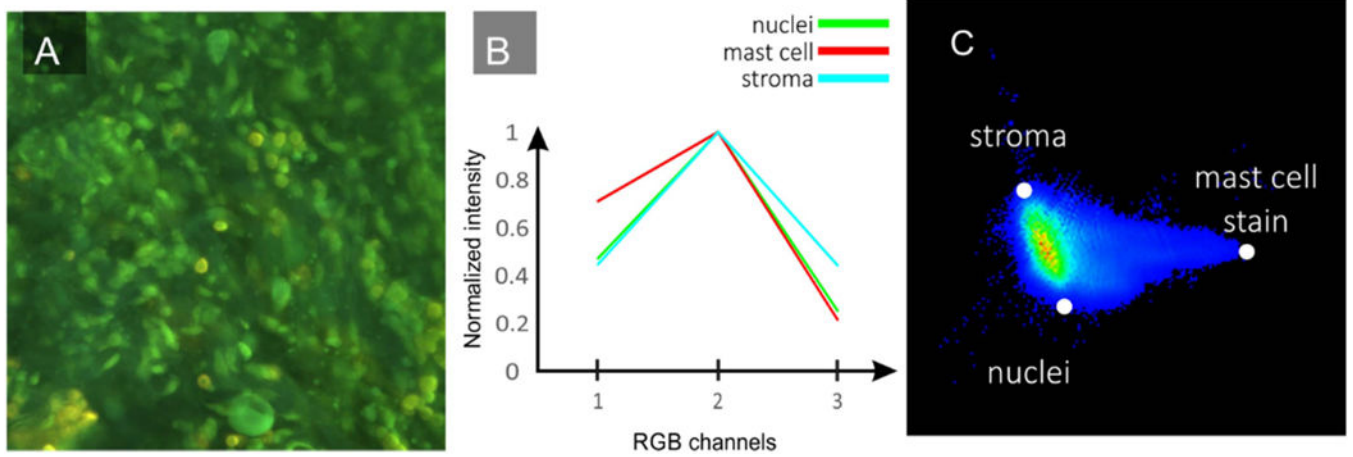
Figure 6.
RGB image of cutaneous mast cell tumors (B) overlapping spectra from stroma, nuclei and cytoplasm and (C) the corresponding phasor plot.
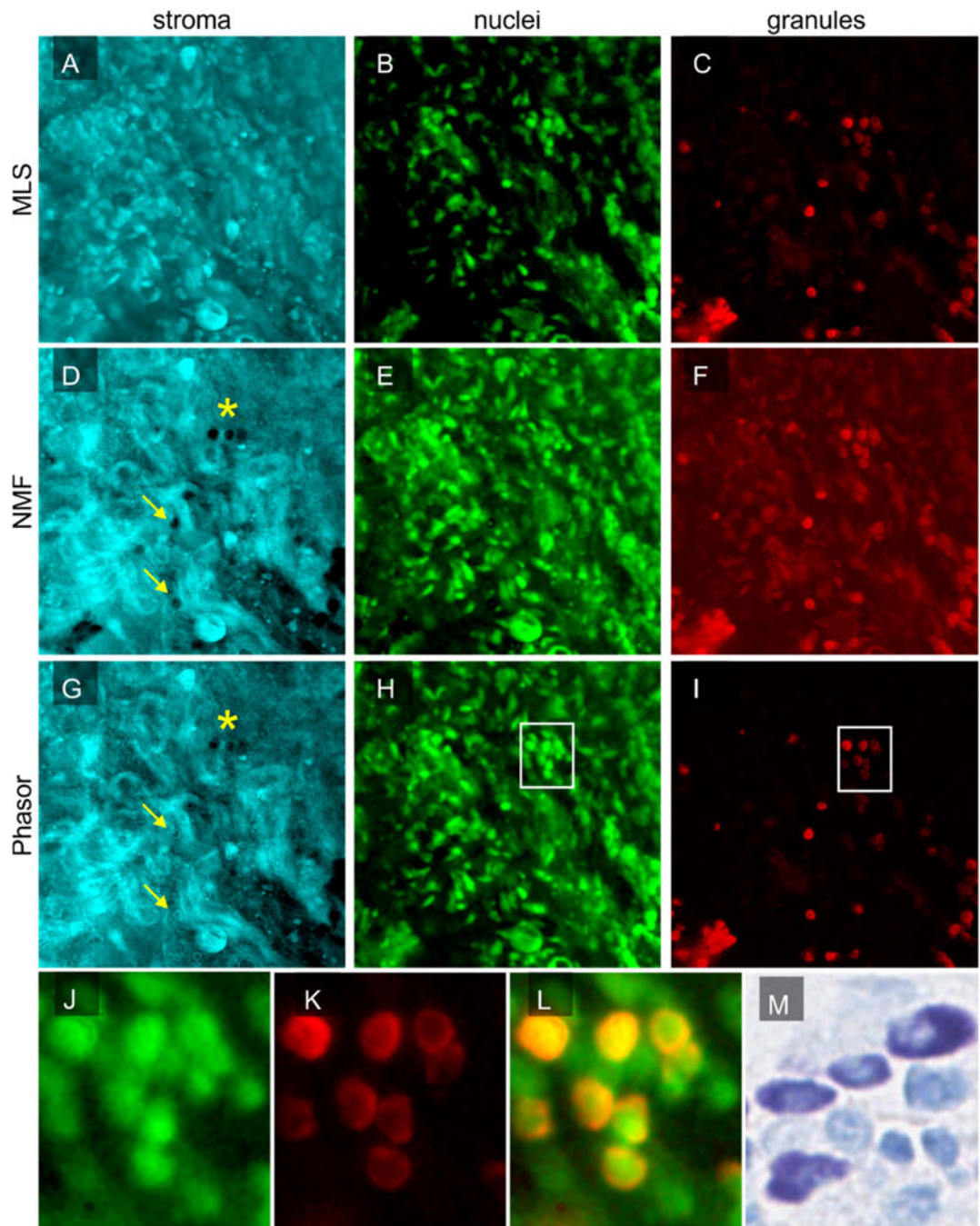
Figure 7.
Comparison of unmixing results from MLS ((A)–(C)), NMF ((D)–(F)) and phasor approach ((G)–(I)). Yellow arrows on (D) and G) show the regions where the cross talk from nuclei is maximum. (J) and (K) are zoomed in images of the white rectangle from (H) and (I), respectively. (L) The overlay image of (J) and (K). (M) Image of same tissue processed through FFPE and stained with toluidine blue—note that granules and nuclei are similarly demonstrated.